

A 1.9-mW 750-kb/s 2.4-GHz F-OOK Transmitter With Symmetric FM Template and High-Point Modulation PLL

Yining Zhang, *Student Member, IEEE*, Ranran Zhou, Woogeun Rhee, *Senior Member, IEEE*, and Zhihua Wang, *Fellow, IEEE*

Abstract—This paper describes a frequency-domain on-off keying (F-OOK) modulation method which utilizes power detection of both a carrier and a sideband by modulating the carrier frequency with a pre-selected modulation template. Compared to on-off keying and binary frequency-shift keying modulations, more efficient bandwidth control is achieved for the same data rate with a symmetric FM template. Since the proposed modulation maintains the average center frequency of the carrier regardless of data pattern, the F-OOK signal can be generated by using only the high-pass modulation path of the conventional phase-locked loop-based two-point modulator, thus relaxing design complexity. A prototype transmitter implemented in 65-nm CMOS consumes 1.9 mW from a 0.8-V supply with a data rate of 750 kb/s, achieving an energy efficiency of 2.5 nJ/b.

Index Terms—CMOS, frequency-shift keying (FSK), low power, modulation, multi-channel, on-off keying (OOK), transmitter, two-point modulator.

I. INTRODUCTION

AS THE power consumption of transceiver front ends cannot be well scaled down with advances in CMOS technology, low-power design with low hardware complexity becomes critical in modern short-range communication systems. Wireless standards such as Bluetooth Low Energy (BLE) and ZigBee (IEEE 802.15.4) have been adopted for low-power short-range transceiver systems [1]–[5]. However, the circuit complexity and power consumption of the existing standards make room for the development of proprietary transceiver systems. For instance, energy-efficient methods such as energy harvesting combined with backscattering [6] and hardware-assisted duty cycling [7] are proposed. Even though those systems could achieve good energy efficiency, link quality and bandwidth efficiency are not well considered. A transmitter based on an injection-locked fractional-N synthesizer achieves high energy efficiency with a decent bandwidth control [8], but using the multi-phase ring oscillator makes it difficult to have the architecture useful for 2.4-GHz applications. Accordingly,

existing modulation and transmission methods need to be first investigated by considering energy efficiency, bandwidth efficiency, and hardware complexity all together.

On-off keying (OOK) or regenerative transceivers are highly power efficient, but they are vulnerable to other interferers and face the difficulty of dc-level calibration or autonomous 0/1 threshold decision, leading to poor link quality and long calibration time [9], [10]. The OOK transmitter also suffers from poor spectrum control, requiring pulse shaping to effectively control the output spectrum [11]. Simple frequency-shift keying (FSK) schemes like binary FSK (BFSK) can relax circuit complexity with noncoherent demodulation yet occupy wider bandwidth than the OOK for the same symbol rate. Complex coherent FSK schemes like Gaussian FSK require dedicated circuitry to provide a precise control of the center frequency and the occupied bandwidth [12]. The common concern of FSK transmitters is center frequency drift due to data pattern, which occurs when the baseband symbols are biased to either 1 or 0 for a certain period. In other words, the average center frequency per symbol of the transmitted signal does not remain the same for arbitrary baseband streams. Hence, a phase-locked loop (PLL)-based modulator such as a digital-intensive phase modulator [13] or a two-point modulator [14], [15] has been used to precisely control the center carrier frequency. In the receiver side, phase-to-digital converter-based architectures [16], [17] or using an auxiliary loop such as the LO carrier recovery loop [18] could also overcome the frequency drift problem.

In this paper, we propose a frequency-domain OOK (F-OOK) modulation method which utilizes power detection of both a carrier and sidebands by modulating the carrier frequency with a pre-selected modulation template. Since the proposed modulation maintains the average center frequency of the carrier regardless of data pattern, the F-OOK transmitter architecture is simplified by employing only high-pass modulation of the conventional PLL-based two-point modulator, named as a high-point modulator or a 1^+ -point modulator. To overcome the nonlinearity of a digitally controlled oscillator (DCO) under low supply, a dedicated 1-bit high-pass modulation mode with a finite-impulse response (FIR) filtering can also be enabled for DCO modulation [15], [19].

This paper is organized as follows. Section II explains the basic operation principle of the F-OOK modulation method and discusses performance comparison with other existing transmission methods. In Section III, F-OOK system

Manuscript received February 20, 2017; revised April 30, 2017; accepted May 26, 2017. Date of publication July 7, 2017; date of current version September 21, 2017. This paper was approved by Guest Editor Deog-Kyoon Jeong. This work was supported in part by the Huawei Innovation Research Program (HIRP) project under Grant YB2015120073. (*Corresponding author: Woogeun Rhee.*)

The authors are with the Institute of Microelectronics, Tsinghua University, Beijing, China, and also with the Tsinghua National Laboratory for Information Science and Technology, Tsinghua University, Beijing 100084, China (e-mail: wrhee@tsinghua.edu.cn).

Color versions of one or more of the figures in this paper are available online at <http://ieeexplore.ieee.org>.

Digital Object Identifier 10.1109/JSSC.2017.2713518

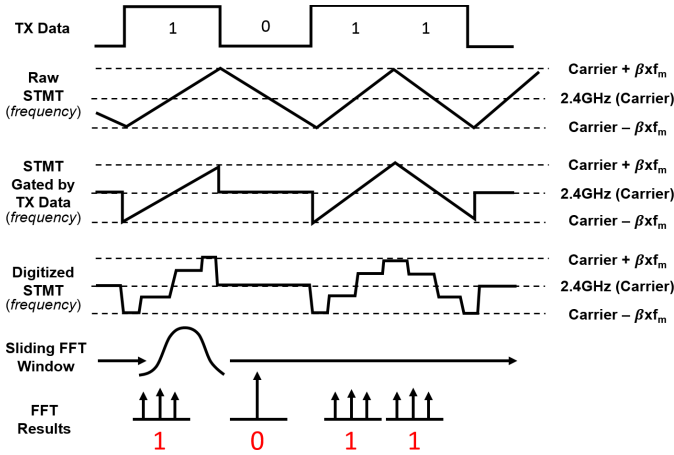


Fig. 1. F-OOK modulation with STMT.

design considerations, including key parameters of defining the modulation template are discussed. In Section IV, the implementation of the F-OOK transmitter is described. Section V shows the experimental results, followed by conclusions in Section VI.

II. F-OOK MODULATION

A. Basic Principles

Fig. 1 shows the basic operation principle of the proposed F-OOK method. The F-OOK modulation scheme uses a pre-defined symmetric triangular modulation template (STMT) to achieve good bandwidth efficiency by occupying narrower bandwidth than the BFSK and the OOK modulations. With the symmetric template, the F-OOK modulation guarantees that the majority of the transmitted signal power remains either on the carrier frequency or on sidebands according to the baseband symbols. By performing power detection of both the carrier and the sidebands, the baseband symbol could be recovered. The shape of the STMT shown in Fig. 1 is determined by considering the maximum frequency deviation, bandwidth efficiency, and demodulation complexity. The maximum frequency deviation is determined by a modulation index. The template is gated by baseband data with a rule as follows: when “1” is sent, the frequency of the transmitted signal changes according to the template; when “0” is sent, the frequency of the transmitted signal stays at the center frequency.

Since the modulation input of the two-point modulator based on the $\Delta\Sigma$ PLL is digital, the gated STMT is digitized with oversampling as depicted in Fig. 1. For demodulation, a sliding fast Fourier transform could be used to distinguish the different spectra of “1” and “0” based on the amplitudes of sidebands and center carrier frequency. When a conventional demodulation architecture similar to the direct-conversion BFSK receiver is employed, a data-pattern-dependent dc offset problem which is present in the conventional BFSK receiver does not occur in the F-OOK receiver since the F-OOK offers a fully balanced binary frequency modulation.

B. Comparison With Existing Techniques

The proposed F-OOK modulation technique enables flexible transceiver design in trade-offs between the energy efficiency

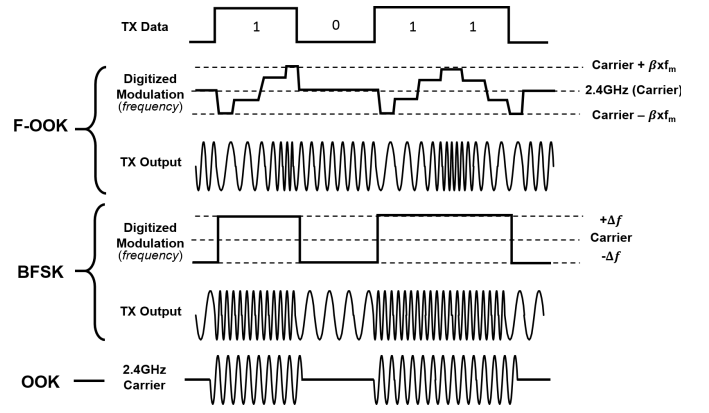


Fig. 2. F-OOK in comparison with BFSK and OOK.

TABLE I
COMPARISON OF F-OOK, OOK, AND BFSK

	F-OOK	OOK	BFSK
Constant Envelope	Yes	No	Yes
Modulation Profile	STMT	Pulse Shape	Pulse Shape
Data Pattern Independent f_{cavg}^*	Yes	Yes	No
Bandwidth Occupation	1 x DR (20dB)	$\sim 2 \times DR$	$\sim 3 \times DR$ (noncoherent)

* f_{cavg} : average center frequency of RF signal

and the bandwidth efficiency. Fig. 2 shows the time domain comparison of the F-OOK, the OOK and the BFSK. The F-OOK signal has a constant envelope, and the average frequency per symbol interval is always the center carrier frequency. In the frequency domain, the F-OOK not only measures the carrier power like the OOK but also uses sidebands to represent corresponding baseband symbols with fully balanced frequency modulation. The bandwidth control of the F-OOK relies on the shape of the STMT and the modulation index together. As in the case of the BFSK, the F-OOK modulation index is relevant to the bandwidth efficiency and the performance of the receiver. When -20 dB bandwidth is assumed, the bandwidth of the F-OOK signal is 50% narrower than that of the noncoherent BFSK for the same data rate. Table I shows a comparison of the F-OOK modulation with the OOK and the BFSK.

III. KEY PARAMETERS OF F-OOK MODULATION

A. Modulation Index

The selection of the modulation index is important in determining bandwidth, demodulation complexity, and receiver sensitivity. When a high modulation index is chosen, the carrier is suppressed by high sidebands, making it easy to

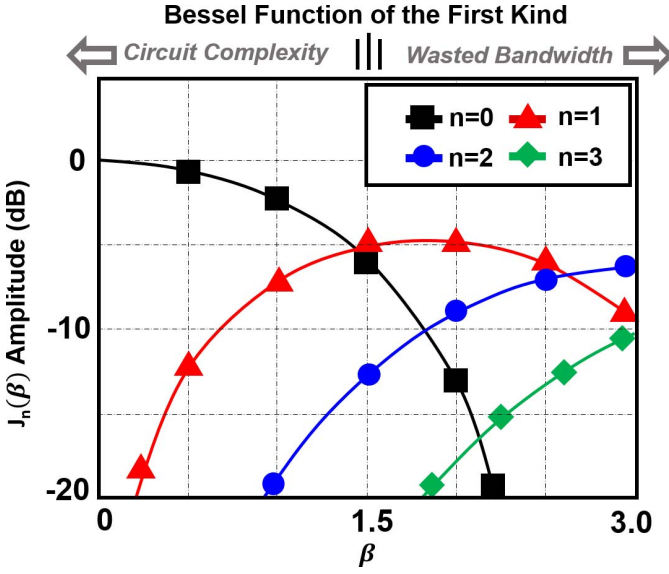


Fig. 3. Sideband amplitudes over different modulation indexes.

distinguish baseband symbols. The modulation index in frequency modulation determines the spectrum shape and the amplitudes of each sideband. The modulation index β is defined by

$$\beta = \frac{\Delta f}{f_m} \quad (1)$$

where Δf is the peak frequency deviation and f_m is the modulation frequency. A frequency modulated signal $s(t)$ with the center frequency f_c and the modulation index β can be expressed by Bessel function series with argument β , that is

$$s(t) = \sum_{n=-\infty}^{\infty} J_n(\beta) \cos(2\pi(f_c + n f_m)t) \quad (2)$$

where $J_n(\beta)$ is the n th order Bessel functions of the first kind given by

$$J_n(\beta) = \sum_{k=0}^{\infty} \left((-1)^k \frac{\left(\frac{1}{2}\beta\right)^{n+2k}}{k!(n+k)!} \right). \quad (3)$$

Fig. 3 shows the amplitudes of different orders of the Bessel functions of the first kind. When β is sufficiently small, the sidebands are negligible except the first-order sideband, which is the case for narrowband FM whose bandwidth is approximately $2f_m$. In this paper, we choose an optimum β in such a way that the carrier, or zeroth order sideband, and the first-order sidebands are the same. That is, the carrier and the first sidebands have nearly the same amplitude, so that the demodulation could be performed by comparing the magnitude of these components. From the plot in Fig. 3, β of around 1.5 is chosen as an optimum value.

Since the second-order sideband level of -13 dBc could give poor adjacent channel rejection, a different modulation template, the STMT, is considered for the F-OOK modulation. The effective modulation frequency with the STMT is half of the actual data rate as depicted in Fig. 1. Hence, the

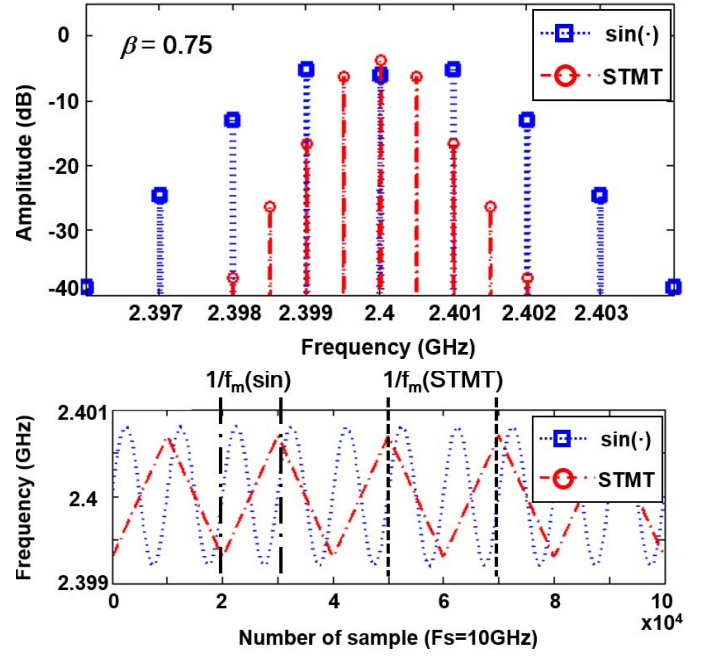


Fig. 4. FM with sinusoidal modulation template and STMT: (a) frequency variation (b) amplitudes of carrier and sidebands with baseband signal set to all “1”.

modulation index with the STMT β_{STMT} is given by

$$\beta_{\text{STMT}} = \frac{\Delta f}{f_{\text{STMT}}} = \frac{\Delta f}{0.5 \times f_b} = 2\beta \quad (4)$$

where f_{STMT} is the STMT frequency and f_b is the baseband data rate. From Fig. 3, the optimum β_{STMT} for the F-OOK modulation can be approximately set to 1.5 since the STMT modulation is close to a discrete sinusoidal modulation. Therefore, the effective value of the optimum β for the F-OOK modulation becomes 0.75, showing 50% reduction of the modulation bandwidth for the same data rate.

B. Template Selection

As discussed, a symmetric triangular wave, namely, the STMT is proposed to have good bandwidth efficiency as well as high adjacent channel rejection. The STMT gives lower second-order spur than the sinusoidal modulation template. In the STMT, either a rising or a falling slope T_{slope} occupies half of the modulation period ($=1/f_{\text{STMT}}$), which is equivalent to a symbol period. That is

$$f_{\text{STMT}} = \frac{1}{2} f_{\text{symbol}} = \frac{1}{2} \times \frac{1}{T_{\text{slope}}} \quad (5)$$

where f_{symbol} is a symbol rate. Fig. 4 shows a comparison of the STMT with the sinusoidal modulation. Unlike the sinusoidal signal where one period stands for one baseband symbol period, each slope of the STMT stands for one symbol as shown in Fig. 4(a). Amplitudes of carrier and sidebands with the baseband signal set to all “1”s are also shown in Fig. 4(b). The spectrum of the transmitted signal modulated by the STMT has lower second-order sidebands below -17 dBc. When the baseband data are driven by a pseudorandom bit sequence (PRBS) instead of all “1”s,

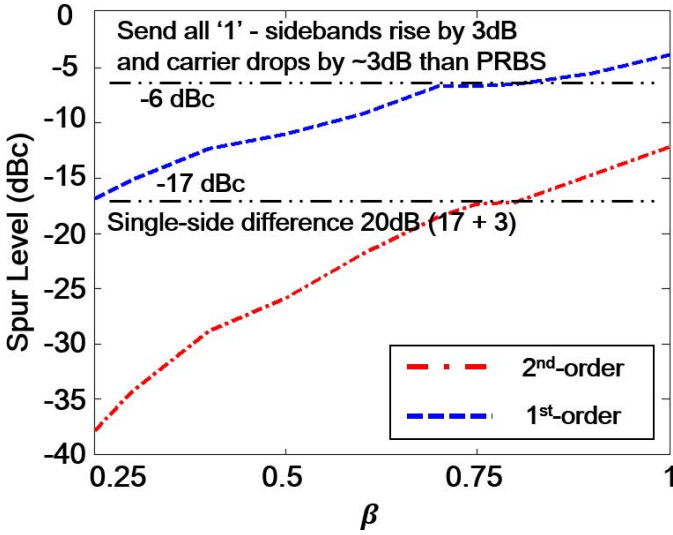


Fig. 5. Sideband power of first- and second-order spurs over different modulation index.

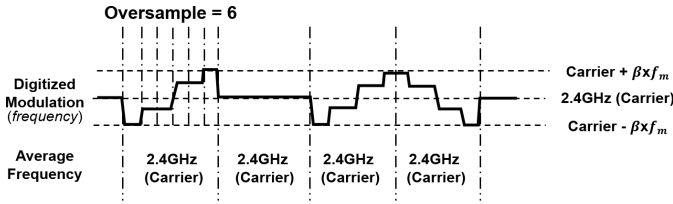


Fig. 6. Digitized STMT.

additional 3-dB reduction is obtained, making sidebands fall below -20 dBc. F-OOK modulation with higher β can be done at the cost of degraded bandwidth efficiency or with more complex modulation template to further suppress sidebands.

Fig. 5 shows the plot of the sideband levels. The sideband levels are calculated on dual sides. The -20 dB single-side rule results in -17 dBc dual side in Fig. 5. Since Fig. 5 is given when the modulator is driven by the PRBS, thus in the “1” interval, the carrier drops and sidebands rise by 3 dB. The -6 dBc line denotes the level when in the “1” interval the carrier and sideband power becomes equal. As could be seen the -6 and -17 dBc line both illustrates an optimum modulation index of around 0.75. Values lower than 0.75 have lower higher-order sidebands, but the first-order sideband is also lower, making it more difficult to perform demodulation.

C. Template Digitization

For two-point modulation based on the digital-intensive PLL, the DCO modulation profile must be digital. Accordingly, the STMT needs to be digitized. Fig. 6 shows an example. Since the high-pass modulation path in the two-point modulator modulates the output frequency as a high-pass filter, the oversampling clock for template digitization should be selected higher than the cutoff frequency of the high-pass modulator. The required system clock frequency f_{clk} for the given oversampling frequency $f_{\text{oversample}}$ is given by

$$f_{\text{clk}} = f_{\text{symbol}} \times f_{\text{oversample}}. \quad (6)$$

Considering a maximum potential symbol rate of 10 Mb/s, digital synthesis complexity, and modulation performance, an oversampling ratio of 6 is chosen. In fact, the series expansion of the standard frequency modulation can be obtained through the trigonometric sum-to-product identities of a basic Bessel function expansion

$$\begin{aligned} \cos(\beta \sin \theta) &= J_0(\beta) + 2 \sum_{k=1}^{\infty} J_{2k}(\beta) \cos(2k\theta) \\ \sin(\beta \sin \theta) &= 2 \sum_{k=0}^{\infty} J_{2k+1}(\beta) \sin((2k+1)\theta). \end{aligned} \quad (7)$$

Let the quantization noise, template signal and digitized template signal be $n(t)$, $x_m(t)$ and $x_{\text{dm}}(t)$, respectively. The relationship between the three signals would be

$$x_m(t) = x_{\text{dm}}(t) + n(t). \quad (8)$$

With the digitized STMT, the expression of the signal $s_m(t)$ using the digital STMT as the frequency modulator, considering quantization error, could be written as

$$\begin{aligned} s_m(t) &= \cos\left(2\pi f_c t + \beta C_0 \int_0^t (x_m(\tau) - n(\tau)) d\tau\right) \\ &= \cos\left(2\pi f_c t + \beta C_0 \int_0^t x_m(\tau) d\tau\right) \cos\left(\beta C_0 \int_0^t n(\tau) d\tau\right) \\ &\quad + \sin\left(2\pi f_c t + \beta C_0 \int_0^t x_m(\tau) d\tau\right) \sin\left(\beta C_0 \int_0^t n(\tau) d\tau\right) \end{aligned} \quad (9)$$

where C_0 is a standalone constant proportional to f_m , which in our case is fixed to be $2f_{\text{symbol}}$. Note that in (9) the term

$$\cos\left(2\pi f_c t + \beta C_0 \int_0^t x_m(\tau) d\tau\right) \quad (10)$$

is the original un-digitized STMT modulated signal. Since the digitization method is used, we could perform digitization in such a way that the integral over one symbol period be 0, in which case the integral below is bounded, that is

$$\int_0^t n(\tau) d\tau = A_n n_{\text{int}}(t) \quad (11)$$

where A_n is the amplitude of the integration result, and $n_{\text{int}}(t)$ stands for the periodical component. $n_{\text{int}}(t)$ satisfies the following conditions:

$$n_{\text{int}}\left(t + \frac{1}{f_{\text{symbol}}}\right) = n_{\text{int}}(t) \quad |n_{\text{int}}(t)| = 1. \quad (12)$$

The decomposition in (11) is possible because the integrated quantized error has a period of $1/f_b$. As the oversampling ratio increases, A_n decreases with reduced quantization noise. When A_n is sufficiently small, (9) could be rewritten as

$$\begin{aligned} s_m(t) &\approx \cos\left(2\pi f_c t + \beta C_0 \int_0^t x_m(\tau) d\tau\right) \\ &\quad + \sin\left(2\pi f_c t + \beta C_0 \int_0^t x_m(\tau) d\tau\right) \beta C_0 A_n n_{\text{int}}(t). \end{aligned} \quad (13)$$

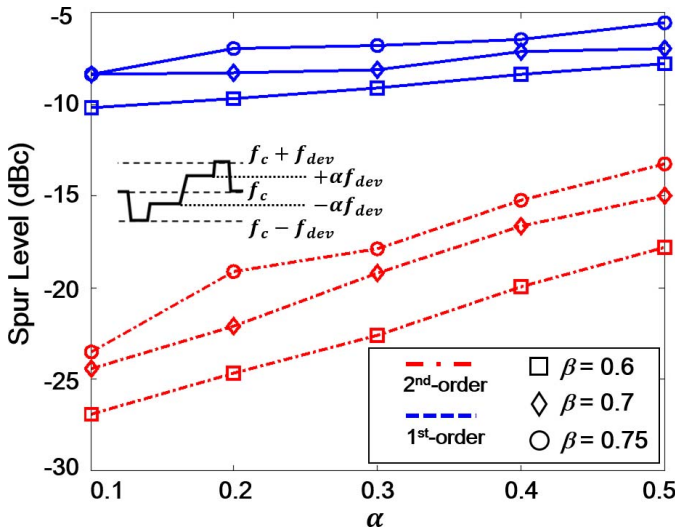


Fig. 7. Sideband power of first- and second-order sidebands over different STMT shape indexes. (PRBS baseband data are assumed).

The first cosine component at the right-hand side in (13) is the original STMT signal itself, and the second component is noise related. Combining (7) and (13), the noise component creates some extra energy on integer times of f_m following the distribution of Bessel function of the first kind where energy decreases logarithmically with a number of orders. The noise component on nf_m is also relative to the Fourier expansion of $x_m(t)$ and $n_{\text{int}}(t)$, proportional to the noise amplitude given that $n_{\text{int}}(t)$ is periodical.

Fig. 6 shows one solution of the digitization of STMT with the oversampling ratio of 6. The discrete digitized modulation template function $X_{\text{dm}}(n)$ is

$$X_{\text{dm}}(n) = \begin{cases} -\Delta f & n = 1 \\ -\alpha \Delta f & n = 2, 3 \\ \alpha \Delta f & n = 4, 5 \\ \Delta f & n = 6. \end{cases} \quad (14)$$

The constant α , the STMT shape index, is positive and less than 1. It could be selected to meet different requirements of sidebands. For instance, larger α would result in higher sidebands, enabling easier demodulation algorithms and wider bandwidth occupation, and vice versa. In practice, α value of 0.1 to 0.5 could be used depending on the modulation index selected.

Fig. 7 shows the sideband power level over the STMT shape index with different modulation indexes. Larger α results in higher sideband power and easier demodulation, but higher-order sidebands tend to increase at the same time. In practice, the value of α is chosen together with an optimum modulation index to control the shape of the output spectrum.

IV. TRANSMITTER IMPLEMENTATION

A. High-Point Modulation

Traditional transmitter design usually includes a polar transmitter for low-power operations with flexibility to work under different standards and scenarios [20]–[22]. In the case of

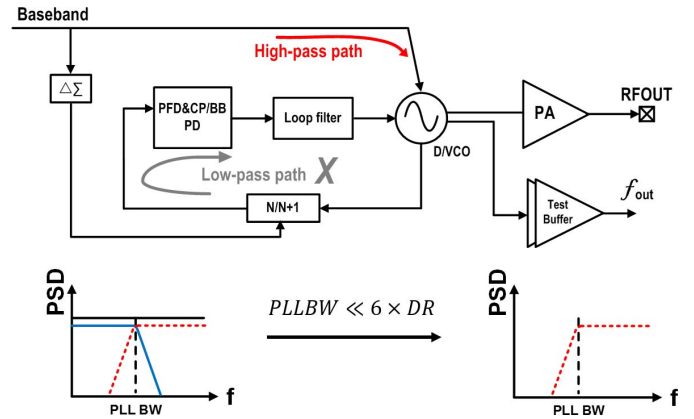


Fig. 8. High-point modulation by disabling low-pass modulation path of two-point modulator.

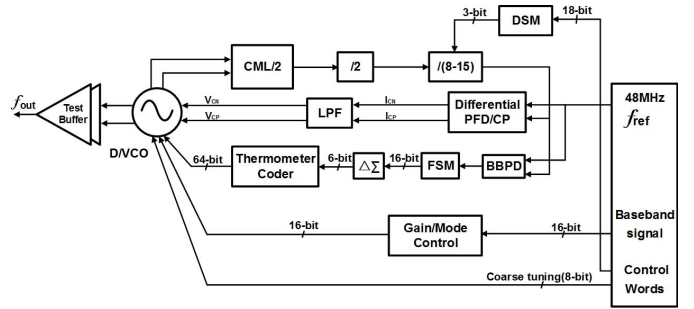


Fig. 9. Block diagram of proposed F-OOK transmitter.

constant envelope modulation, the polar transmitter does not need to accommodate the amplitude modulation components, leaving only the frequency modulation circuitry. The $\Delta\Sigma$ PLL-based two-point modulator with high- and low-pass paths matched has a uniform modulation sensitivity regardless of the PLL bandwidth [13]–[15]. A phase rotator based modulation is also proposed, yet requires high data clock of the rotator block and limits scalability [23]. Direct frequency modulation without requiring accurate frequency control could be used, but it suffers from serious process, voltage and temperature variations [24]. Quadrature frequency synthesizers are also used in the transmitter at the cost of increased inductor area [25].

As discussed previously, the digitized STMT does not contain any dc component, thus making high-pass-only modulation (high-point modulation) possible. As shown in Fig. 8, we employ a traditional two-point modulator and disable the low-pass modulation. The PLL controls the center frequency of the carrier and the F-OOK modulation is performed by using only the high-pass modulation path of the conventional two-point modulation. Hence, the $\Delta\Sigma$ modulator in the low-pass path only takes a constant channel selection signal without any modulation information. One benefit of using the high-point modulation over the conventional two-point modulation is that the gain match between the high-pass and the low-pass modulation paths is not needed.

B. Transmitter Design

Fig. 9 shows the block diagram of the proposed transmitter in which the F-OOK modulation is done by the high-point

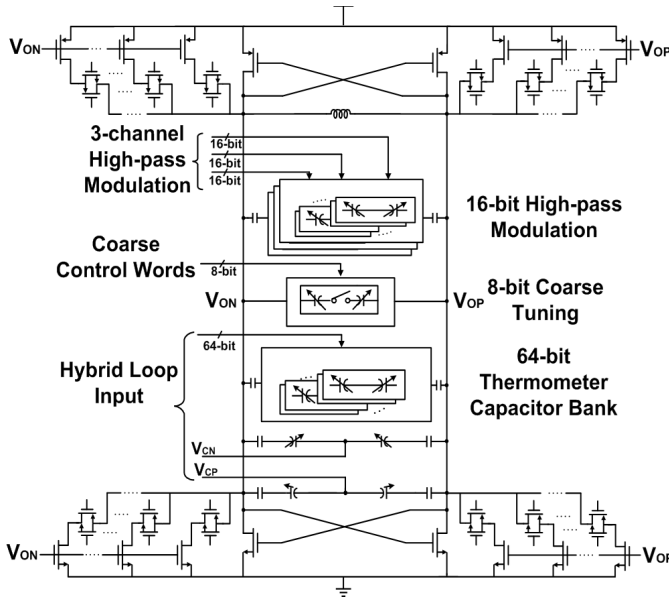


Fig. 10. Schematic of low-voltage D/VCO.

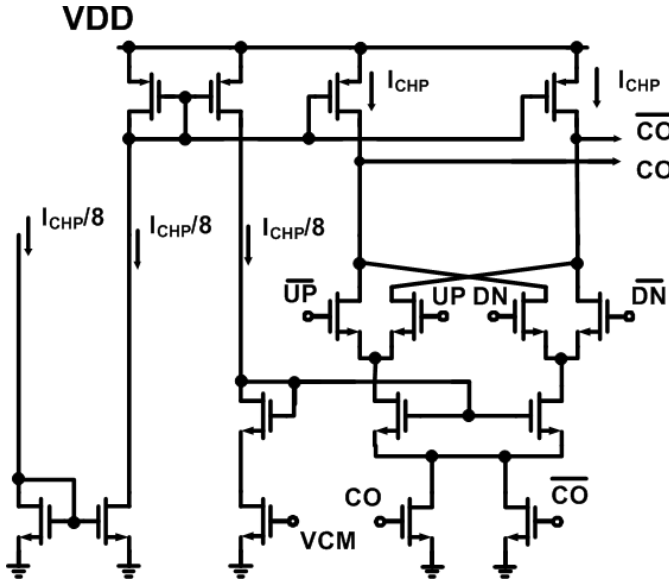


Fig. 11. Schematic of low-voltage differential charge pump.

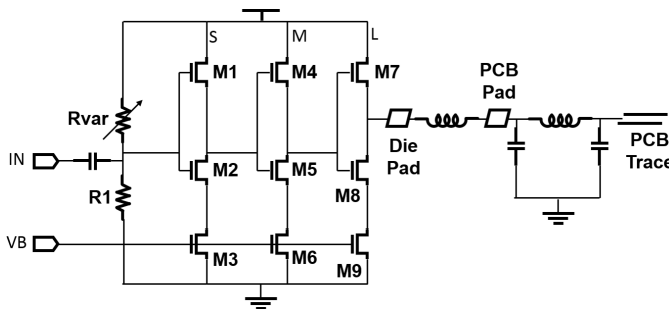


Fig. 12. Schematic of inverter-based PA.

modulation PLL, covering the 2.4-GHz industrial, scientific and medical band. Frequency division ratio ranges from 32 to 60 with a reference frequency of 48 MHz. Since the time-to-digital converter suffers from poor resolution and linearity

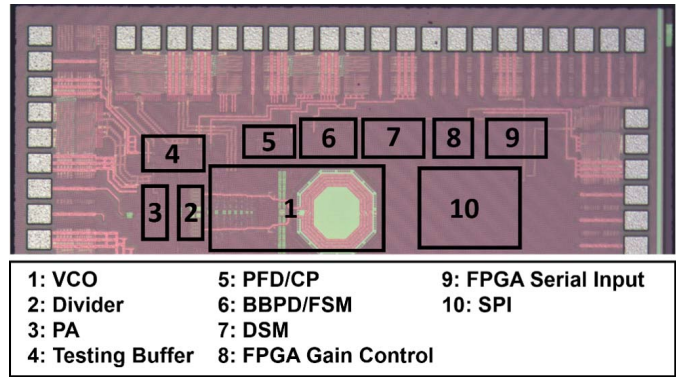


Fig. 13. Chip micrograph.

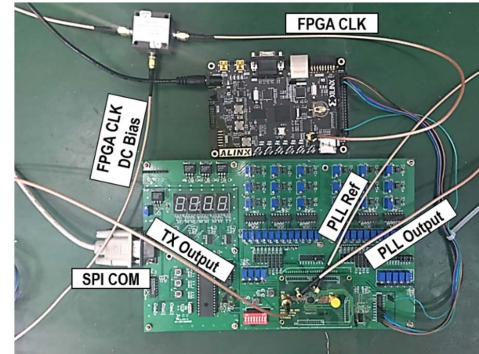
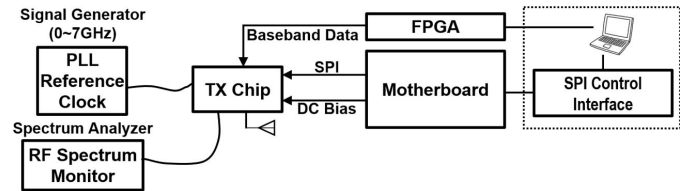


Fig. 14. Testing diagram and motherboard connection.

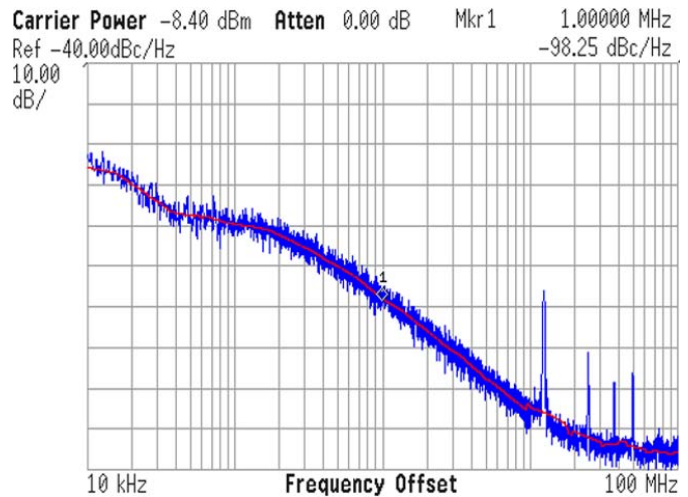


Fig. 15. Measured PLL phase noise.

in the worst corner with <1 V supply, a hybrid PLL architecture with the digital/voltage-controlled oscillator (D/VCO) is designed [15]. The corner frequency of the low-pass filter in the analog proportional-gain path is set to be much less than $6f_{\text{symbol}}$ as required by the high-point modulation.

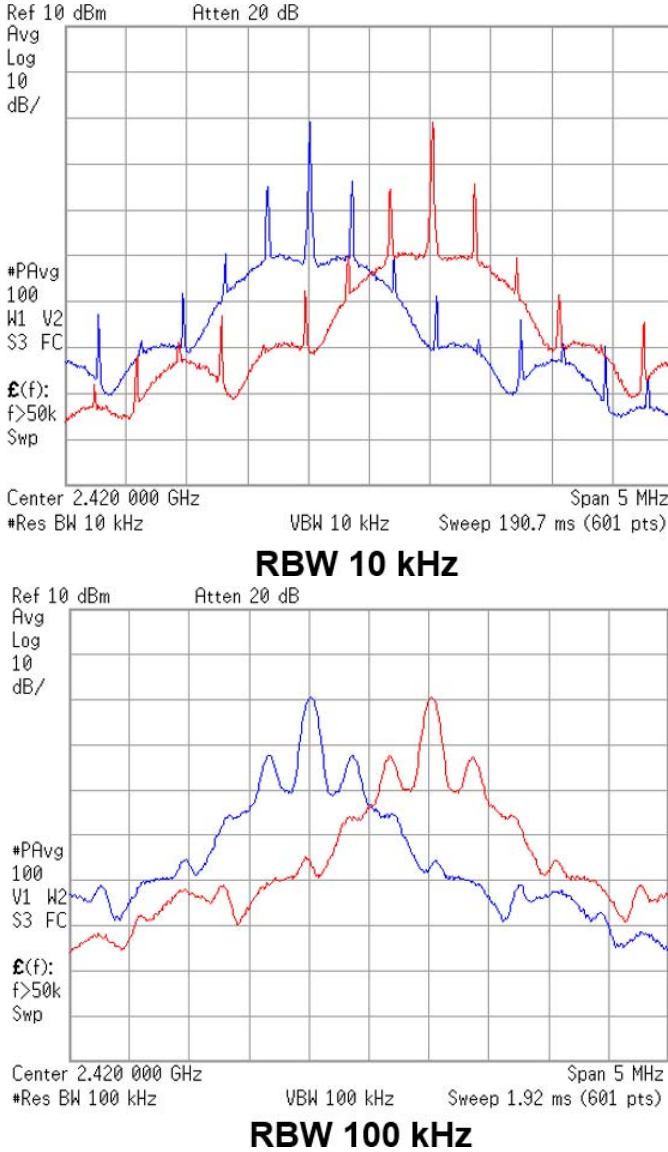


Fig. 16. Measured dual-channel output spectrum of F-OOK transmitter with different settings: (a) RBW 10 kHz; (b) RBW 100 kHz.

To mitigate the D/VCO nonlinearity, the FIR-embedded 1-bit $\Delta\Sigma$ modulation is employed for the high-pass modulation path in the D/VCO [15]. High-point data are scaled by a gain control block to cover different frequency deviations before directly controlling the thermometer-coded high-pass modulation capacitors in the D/VCO. The baseband signal is generated by a field-programmable gate array (FPGA). The D/VCO output signal is fed to a constant envelope power amplifier (PA).

C. Circuit Design

Fig. 10 shows the schematic of the low-voltage D/VCO. To achieve low-voltage operation, no tail current mirror is used [19]. Instead, programmable loads and cross-coupled pairs are designed. A 64-bit fine control capacitor array is designed for the digital input path, and an analog varactor is used for the analog input path. The 16-bit high-pass capacitor array consists of three independent capacitor

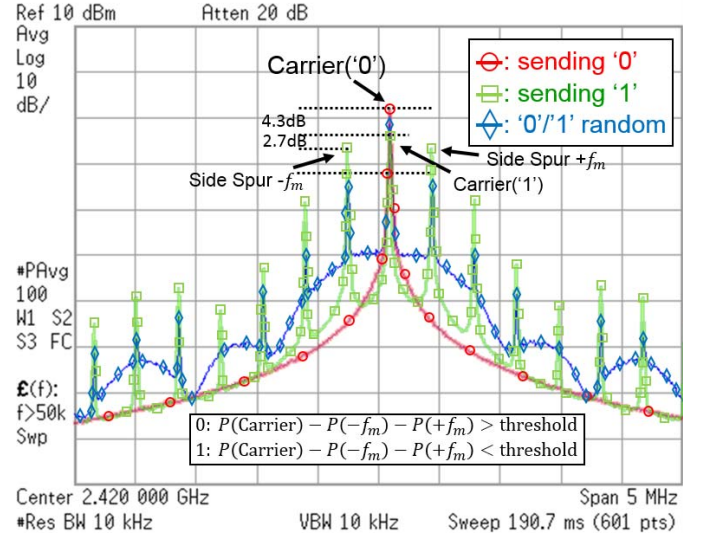


Fig. 17. Measured output spectrum of transmitting random baseband symbols, all “0” and all “1”.

arrays, each having 16 identical capacitor cells. Each capacitor array provides different peak frequency deviations. The 16-bit high-pass capacitors array can be controlled either by a 16-tap FIR filter after the 1-bit $\Delta\Sigma$ modulator or by direct baseband modulation. The cell capacitance can be configured by MOS capacitors with 0.3, 2.0, and 8.1 fF to have frequency deviations of 1, 7, and 30 MHz, respectively, which is set by the gain control block. The D/VCO is designed to have a tuning range of 2.1-to-2.5 GHz to ensure the coverage of the 2.4-GHz ISM band, consuming 0.9 mW from a 0.8-V supply.

Fig. 11 shows the schematic of a differential charge pump. The charge pump is designed in fully differential to have good linearity under low-voltage operation and minimize the supply and substrate noise coupling. An NMOS transistor pair at the bottom are in triode region and used for common-mode feedback to set the common-mode voltage V_{CM} of the differential charge pump.

Fig. 12 shows the schematic of the inverter-based PA for a constant envelope signal. Three-stage inverter amplifiers are sized with increasing ratio. The dc level of the input is set by two resistors, R_{var} and R_1 , where R_{var} is controlled by the serial-to-parallel interface and an optimum value is set during initial calibration. The bias current is tunable from 20 to 100 μ A and power consumption ranges from 200 to 520 μ W with an output power ranging from -40 to -9 dBm. The worst-case IIP3 is 15 dBm in the simulation.

V. EXPERIMENTAL RESULTS

A prototype of 2.4-GHz F-OOK transmitter is implemented in 65-nm CMOS. The chip micrograph is shown in Fig. 13. The core area is 1.0 mm by 0.41 mm. The transmitter consumes 1.9 mW with 0.8 V supply at 750 kb/s. The PLL lock-in range of 2.11-to-2.52 GHz is measured. Fig. 14 shows a testing diagram and motherboard connection for transmitter testing. The FPGA is used for data modulation and the SPI control interface is used for online programming and parameter setting.

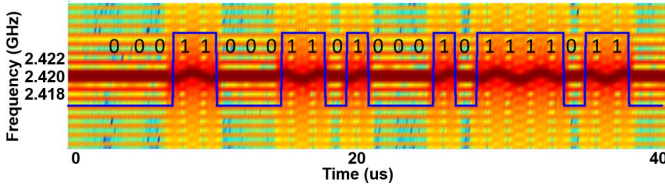


Fig. 18. Measured spectrogram of F-OOK transmitter output.

TABLE II

PERFORMANCE SUMMARY IN COMPARISON WITH EXISTING WORKS

	This Work	ISSCC 2012 [1]	ISSCC 2013 [5]	ISSCC 2014 [14]	ASSCC 2014 [19]
Technology	65nm	130nm	90nm	40nm	65nm
Core Area(mm ²)	0.41	5.9	2	0.2	0.47
Supply (V)	0.8	1	1.2	1	0.65
RF Freq.	2.4GHz	2.4GHz	2.4GHz	2.1-2.7GHz	2.4G/400MHz
Modulation Scheme	F-OOK	GFSK	GFSK HSOQPSK DQPSK	GFSK HSOQPSK	GFSK OQPSK
Data Rate	750kb/s	1Mb/s	2Mb/s (HSOQPSK) 1Mbps (GFSK)	2Mb/s	1Mb/s
TX Output (Typ.) (dBm)	-10	-30 to -3	0	(PLL Only)	(PLL Only)
Power Consumption	1.9mW	4.6mW (Out: -10dBm)	5.4mW	0.86mW	0.9mW (2.4GHz)
Energy Efficiency	2.5nJ/b	4.6nJ/b	2.7nJ/b (HSOQPSK) 5.4nJ/b (GFSK)	(PLL Only)	(PLL Only)

Fig. 15 shows the measured PLL phase noise performance at 2.4-GHz output. The reference frequency of 49.6 MHz is used with the frequency division ratio of 48.39. The in-band phase noise of -79.6 dBc/Hz at 100-kHz offset frequency and out-of-band phase noise of -98.25 dBc/Hz at 1-MHz frequency offset are measured. The PLL loop bandwidth is about 200 kHz.

Fig. 16 shows the measured output spectrum with 750-kb/s F-OOK modulation with the resolution bandwidth (RBW) of 10 and 100 kHz. The frequency deviation is set to have 550 kHz in the high-pass modulation path according to design parameters. Since the high-pass modulation path has 16-bit thermometer-coded switched capacitors for fine control, the modulation performance with the digitized STMT differs from that with an ideal STMT. As observed in Fig. 16, the first-order sidebands occur at 375 kHz, half of the data rate. The channel bandwidth, with -20 dB bandwidth assumption, is nearly equivalent to the data rate and out-of-channel spurs fall below -40 dBc at 1.5 times of the single-side bandwidth. The measured output spectrum with random baseband symbols, all “0” symbols and all “1” symbols, are shown in Fig. 17. The different distribution of the carrier frequency component and sidebands makes demodulation possible by detecting the energy difference of frequency components.

Fig. 18 shows the measured spectrogram of the transmitter output. The baseband signal is overlapped onto the

spectrogram which is calculated through real-time signal collected by a 10-G-sample/s oscilloscope. The darker color indicates higher power concentration and vice versa. For example, the center frequency with the highest power (darkest) is changing according to the F-OOK scheme, modulated by the STMT when sending “1” and unmodulated when sending “0”. As clearly seen, the transmitted frequency changes according to the digitized STMT as expected, proving the correct function of the F-OOK modulation.

The 750-kb/s TX consumes 1.9 mW under 0.8-V supply. The high-point modulation PLL and the PA consume 1.4 and 0.5 mW, respectively. The measured performance in comparison with other state-of-the-art transmitters is shown in Table II.

VI. CONCLUSION

A 0.8-V 2.4-GHz 750-kb/s F-OOK transmitter is fabricated in 65-nm CMOS. The proposed F-OOK modulation offers a good design trade-off compared to the OOK and the BFSK modulation methods. The F-OOK transmitter does not require two-point modulation. By utilizing the high-pass modulation PLL, no matching with the low-pass modulation is required. The measured F-OOK spectrum has a 20-dB bandwidth of 780 kHz measured at 10-kHz RBW and 910 kHz at 100-kHz RBW. The measured spectrogram shows that the F-OOK modulation is performed correctly. The 750-kb/s F-OOK transmitter consumes 1.9 mW from a 0.8-V supply.

REFERENCES

- [1] A. Wong *et al.*, “A 1 V 5 mA multimode IEEE 802.15.6/bluetooth low-energy WBAN transceiver for biotelemetry applications,” in *IEEE Int. Solid-State Circuits Conf. (ISSCC) Dig. Tech. Papers*, Feb. 2012, pp. 300–301.
- [2] Y.-H. Liu *et al.*, “A 3.7 mW-RX 4.4 mW-TX fully integrated bluetooth low-energy/IEEE802.15.4/proprietary SoC with an ADPLL-based fast frequency offset compensation in 40 nm CMOS,” in *IEEE Int. Solid-State Circuits Conf. (ISSCC) Dig. Tech. Papers*, Feb. 2015, pp. 1–3.
- [3] M. Vidojkovic *et al.*, “A 0.33 nJ/b IEEE802.15.6/proprietary-MICS/ISM-band transceiver with scalable data-rate from 11 kb/s to 4.5 Mb/s for medical applications,” in *IEEE Int. Solid-State Circuits Conf. (ISSCC) Dig. Tech. Papers*, Feb. 2014, pp. 170–171.
- [4] X. Wang *et al.*, “A 0.9–1.2 V supplied, 2.4 GHz bluetooth low energy 4.0/4.2 and 802.15.4 transceiver SoC optimized for battery life,” in *Proc. 42nd Eur. Solid-State Circuits Conf. (ESSCIRC)*, Sep. 2016, pp. 125–128.
- [5] Y.-H. Liu *et al.*, “A 1.9 nJ/b 2.4 GHz multistandard (bluetooth low energy/zigbee/IEEE802.15.6) transceiver for personal/body-area networks,” in *IEEE Int. Solid-State Circuits Conf. (ISSCC) Dig. Tech. Papers*, Feb. 2013, pp. 446–447.
- [6] A. Shirane *et al.*, “A 5.8 GHz RF-powered transceiver with a 113 μ W 32-QAM transmitter employing the IF-based quadrature backscattering technique,” in *IEEE Int. Solid-State Circuits Conf. (ISSCC) Dig. Tech. Papers*, Feb. 2015, pp. 1–3.
- [7] A. Paidimarri, N. Ickes, and A. P. Chandrakasan, “A +10 dBm BLE transmitter with sub-400 pW leakage for ultra-low duty cycles,” *IEEE J. Solid-State Circuits*, vol. 51, no. 6, pp. 1331–1346, Jun. 2016.
- [8] K.-H. Teng and C.-H. Heng, “A 370-pJ/b multichannel BFSK/QPSK transmitter using injection-locked fractional-N synthesizer for wireless biotelemetry devices,” *IEEE J. Solid-State Circuits*, vol. 52, no. 3, pp. 867–880, Jan. 2017.
- [9] M. Vidojkovic *et al.*, “A 2.4 GHz ULP OOK single-chip transceiver for healthcare applications,” *IEEE Trans. Biomed. Circuits Syst.*, vol. 5, no. 6, pp. 523–534, Dec. 2011.
- [10] H. Cho *et al.*, “A 79 pJ/b 80 Mb/s full-duplex transceiver and a 42.5 μ W 100 kb/s super-regenerative transceiver for body channel communication,” *IEEE J. Solid-State Circuits*, vol. 51, no. 1, pp. 310–317, Jan. 2016.

- [11] X. Huang, P. Harpe, X. Wang, G. Dolmans, and H. D. Groot, "A 0 dBm 10 Mbps 2.4 GHz ultra-low power ASK/OOK transmitter with digital pulse-shaping," in *Proc. IEEE Radio Freq. Integr. Circuits Symp.*, May 2010, pp. 263–266.
- [12] R. Cavallari, F. Martelli, R. Rosini, C. Buratti, and R. Verdone, "A survey on wireless body area networks: Technologies and design challenges," *IEEE Commun. Surveys Tuts.*, vol. 16, no. 3, pp. 1635–1657, 3rd Quart., 2014.
- [13] G. Marzin, S. Levantino, C. Samori, and A. L. Lacaita, "A 20 Mb/s phase modulator based on a 3.6 GHz digital PLL with –36 dB EVM at 5 mW power," in *IEEE Int. Solid-State Circuits Conf. (ISSCC) Dig. Tech. Papers*, Feb. 2012, pp. 342–344.
- [14] V. K. Chhillara *et al.*, "An 860 μ W 2.1-to-2.7 GHz all-digital PLL-based frequency modulator with a DTC-assisted snapshot TDC for WPAN (Bluetooth Smart and ZigBee) applications," in *IEEE Int. Solid-State Circuits Conf. (ISSCC) Dig. Tech. Papers*, Feb. 2014, pp. 172–173.
- [15] N. Xu, W. Rhee, and Z. Wang, "A hybrid loop two-point modulator without DCO nonlinearity calibration by utilizing 1 bit high-pass modulation," *IEEE J. Solid-State Circuits*, vol. 49, no. 10, pp. 2172–2186, Oct. 2014.
- [16] Y. H. Liu, A. Ba, J. H. C. V. D. Heuvel, K. Philips, G. Dolmans, and H. D. Groot, "A 1.2 nJ/bit 2.4 GHz receiver with a sliding-IF phase-to-digital converter for wireless personal/body area networks," *IEEE J. Solid-State Circuits*, vol. 49, no. 12, pp. 3005–3017, Dec. 2014.
- [17] A. Sai *et al.*, "A 5.5mW ADPLL-based receiver with hybrid-loop interference rejection for BLE application in 65nm CMOS," *IEEE Int. Solid-State Circuits Conf. (ISSCC) Dig. Tech. Papers*, vol. 51, Dec. 2016, pp. 3125–3136.
- [18] W.-Z. Chen, T.-Y. Lu, W.-W. Ou, S.-T. Chou, and S.-Y. Yang, "A 2.4 GHz reference-less receiver for 1 Mbps QPSK demodulation," *IEEE Trans. Circuits Syst. I, Reg. Papers*, vol. 59, no. 3, pp. 505–514, Mar. 2012.
- [19] Y. Li, N. Xu, Y. Zhang, W. Rhee, S. Kang, and Z. Wang, "A 0.65 V 1.2 mW 2.4 GHz/400 MHz dual-mode phase modulator for mobile healthcare applications," in *Proc. IEEE Asian Solid-State Circuits Conf. (A-SSCC)*, Nov. 2014, pp. 261–264.
- [20] Z. Song *et al.*, "A fully-integrated reconfigurable transceiver for narrow-band wireless communication in 180 nm CMOS," in *Proc. IEEE Radio Freq. Integr. Circuits Symp. (RFIC)*, May 2015, pp. 167–170.
- [21] A. Ba *et al.*, "A 1.3 nJ/b IEEE 802.11ah fully-digital polar transmitter for IoT applications," *IEEE J. Solid-State Circuits*, vol. 51, no. 12, pp. 3103–3113, Dec. 2016.
- [22] L. Zhang *et al.*, "A reconfigurable sliding-IF transceiver for 400 MHz/2.4 GHz IEEE 802.15.6/ZigBee WBAN hubs with only 21% tuning range VCO," *IEEE J. Solid-State Circuits*, vol. 48, no. 11, pp. 2705–2716, Nov. 2013.
- [23] Y.-H. Liu, L.-G. Chen, C.-Y. Lin, and T.-H. Lin, "A 650-pJ/bit MedRadio transmitter with an FIR-embedded phase modulator for medical micro-power networks (MMNs)," *IEEE Trans. Circuits Syst. I, Reg. Papers*, vol. 60, no. 12, pp. 3279–3288, Dec. 2013.
- [24] J. Bae, N. Cho, and H.-J. Yoo, "A 490 μ W fully MICS compatible FSK transceiver for implantable devices," in *Proc. IEEE Symp. VLSI Circuits*, Jun. 2009, pp. 36–37.
- [25] H. Jin, D. Kim, and B. Kim, "Efficient digital quadrature transmitter based on IQ cell sharing," in *IEEE Int. Solid-State Circuits Conf. (ISSCC) Dig. Tech. Papers*, Feb. 2015, pp. 168–169.



Yining Zhang (S'16) received the B.S. degree in electronics engineering from Tsinghua University, Beijing, China, in 2013, where he is currently pursuing the Ph.D. degree with the Institute of Microelectronics.

His current research interests include narrowband low-power transceiver and ultra-wideband communication systems for Internet of Things applications.



Ranran Zhou received the B.S. degree in integrated circuit design and integrated systems from Shandong University, Jinan, China, in 2014. She is currently pursuing the M.E. degree in microelectronics with Tsinghua University, Beijing, China.

Her current research interests include phase-locked loops and receiver front-ends for low-power short-range communications.



Woogeun Rhee (M'00–SM'11) received the B.S. degree in electronics engineering from Seoul National University, Seoul, South Korea, in 1991, the M.S. degree in electrical engineering from the University of California, Los Angeles, CA, USA, in 1993, and the Ph.D. degree in electrical and computer engineering from the University of Illinois at Urbana–Champaign, Champaign, IL, USA, in 2001.

From 1997 to 2001, he was a Principal Engineer with Conexant Systems, Newport Beach, CA, where he was developed low-power, low-cost fractional-N synthesizers. From 2001 to 2006, he was with IBM Thomas J. Watson Research Center, Yorktown Heights, NY, USA, where he was involved in clocking area for high-speed I/O serial links, including low-jitter phase-locked loops, clock-and-data recovery circuits, and on-chip testability circuits. In 2006, he joined the faculty as an Associate Professor at the Institute of Microelectronics, Tsinghua University, Beijing, China, and became a Professor in 2011. He holds 23 U.S. patents. His current research interests include short-range low-power radios for next generation wireless systems and clock/frequency generation circuits for wireline and wireless communications.

Dr. Rhee was a recipient of several IBM Research Division Awards during 2001–2006, the IBM Faculty Partnership Award in 2007, and the Advanced Employee Award from Tsinghua University in 2012. He was the co-recipient of the Silkroad Award at the 2008 IEEE ISSCC and the Best Paper Award at the 2014 VLSI-DAT. He has served as a member of several IEEE conferences, including ISSCC from 2012 to 2016, CICC, and A-SSCC. He has been an Associate Editor of the IEEE TRANSACTIONS ON CIRCUITS AND SYSTEMS II: EXPRESS BRIEFS from 2008 to 2009 and a Guest Editor of the IEEE JOURNAL OF SOLID-STATE CIRCUITS Special Issue in 2012 and 2013. He is currently an IEEE Distinguished Lecturer of the Solid-State Circuits Society from 2016 to 2017 and serves as an Associate Editor for the IEEE JOURNAL OF SOLID-STATE CIRCUITS. He has been listed in Marquis *Who's Who in the World* since 2009.



Zhihua Wang (M'99–SM'04–F'17) received the B.S., M.S., and Ph.D. degrees in electronic engineering from Tsinghua University, Beijing, China, in 1983, 1985, and 1990, respectively.

He was a Visiting Scholar at Carnegie Mellon University, Pittsburgh, PA, USA, from 1992 to 1993 and KU Leuven, Leuven, Belgium, from 1993 to 1994, and was a Visiting Professor at the Hong Kong University of Science and Technology, Hong Kong, from 2014 to 2015. He has been a Full Professor and the Deputy Director of the Institute of

Microelectronics, Tsinghua University, since 1997 and 2000. He has co-authored 11 books/chapters, over 160 (439) papers in international journals (conferences), and holds 121 Chinese and 7 U.S. patents. His current research interests include CMOS radio frequency integrated circuit (RFIC) and biomedical applications, involving radio frequency identification, phase-locked loop, low-power wireless transceivers, and smart clinic equipment combined with leading edge RFIC and digital image processing techniques.

Prof. Wang has been a Steering Committee Member of the IEEE A-SSCC since 2005. He has served as an AdCom Member of the IEEE SSCS from 2016 to 2019, a Technology Program Committee Member of the IEEE ISSCC from 2005 to 2011, the Chairman of the IEEE SSCS Beijing Chapter from 1999 to 2009, the Technical Program Chair of the A-SSCC 2013, a Guest Editor of the IEEE JSSC Special Issues in 2006, 2009, and 2014, an Associate Editor of the IEEE TRANSACTIONS ON CAS-I, II and the IEEE TRANSACTIONS ON BioCAS, and has held other administrative/expert committee positions in China's national science and technology projects.